Kevin Schillo
Department of Mechanical and
Aerospace Engineering,
University of Alabama in Huntsville,
301 Sparkman Dr NW,
Huntsville, AL 35899

Jason Cassibry
Department of Mechanical and
Aerospace Engineering,
University of Alabama in Huntsville,
301 Sparkman Dr NW,
Huntsville, AL 35899

Mitchell Rodriguez
Department of Mechanical and
Aerospace Engineering,
University of Alabama in Huntsville,
301 Sparkman Dr NW,
Huntsville, AL 35899

Seth Thompson
Department of Mechanical and
Aerospace Engineering,
University of Alabama in Huntsville,
301 Sparkman Dr NW,
Huntsville, AL 35899

Suite for Smooth Particle Hydrodynamic Code Relevant to Spherical Plasma Liner Formation and Implosion

Three-dimensional (3D) modeling of magneto-inertial fusion (MIF) is at a nascent stage of development. A suite of test cases relevant to plasma liner formation and implosion is presented to present the community with some exact solutions for verification of hydrocodes pertaining to MIF confinement concepts. MIF is of particular interest to fusion research, as it may lead to the development of smaller and more economical reactor designs for power and propulsion. The authors present simulated test cases using a new smoothed particle hydrodynamic (SPH) code called SPFMax. These test cases consist of a total of six problems with analytical solutions that incorporate the physics of radiation cooling, heat transfer, oblique-shock capturing, angular-momentum conservation, and viscosity effects. These physics are pertinent to plasma liner formation and implosion by merging of a spherical array of plasma jets as a candidate standoff driver for MIF. An L^2 norm analysis was conducted for each test case. Each test case was found to converge to the analytical solution with increasing resolution, and the convergence rate was on the order of what has been reported by other SPH studies. [DOI: 10.1115/1.4042710]

1 Introduction

Magneto-inertial fusion (MIF) concepts may result in significantly smaller reactors [1] and enable near-term development of propulsion systems [2]. In MIF, a strong magnetic field is used to reduce cross-field thermal transport rates and enhance fusion-product charged-particle energy deposition within an imploded magnetized plasma-fuel target until fusion reactions occur [3,4]. Because of the potential for lower compression power and total stored energy in the fusion plasma, MIF may hold potential as being a low-cost development path for reactors much smaller than reactor concepts that use magnetic confinement or inertial confinement. Additionally, fusion propulsion using MIF approaches as the reactor has been shown by Cassibry et al. [2], Miernik et al. [5], and Adams et al. [6] to rapidly reduce interplanetary trip times compared to conventional propulsion systems.

Among MIF concepts are magnetized target fusion using solid [7–9] and plasma liners [10–14]. Solid liners have been studied extensively for MIF, with Sandia's MagLIF concept being one of the most prominent examples. In this concept, a pulsed-power machine is used to implode a cylindrical liner onto a magnetized and preheated fusion fuel. One-dimensional (1D) simulations conducted by Slutz et al. [7] found magnetization and preheating of the fusion fuel to be necessary for achieving significant fusion yield with Sandia's Z machine. Two-dimensional (2D) simulations found a liner thickness 10–20% of the radius to be needed to mitigate against magneto-Rayleigh-Taylor instabilities [7]. Further 2D simulations conducted by Slutz et al. [8] found that a hot spot with a sufficiently high areal density was needed for a burn wave to propagate radially through the fusion fuel. A liner aspect ratio of 6 was found to be effective in preventing Rayleigh-Taylor

instabilities. The fusion gain was found to exceed 100 for a current of 60 MA and 1000 for a current of 70 MA [8]. Experiments conducted by Gomez et al. involved a target of deuterium gas premagnetized with a 10 T field, heated by a 2.5 kJ, 1 TW laser, and imploded by a 19 MA current. The experiment resulted in deuterium-deuterium and secondary deuterium-tritium fusion reactions. These experiments verified the MagLIF's capability to achieve fusion conditions with laser heating and magnetization, as well as compressing a seed magnetic field [9].

MagLIF is challenged by the lack of reusability of the liner implosion system and close proximity of the driver hardware to the burning plasma. Following solid liner implosion, debris may also be deposited on the interior wall of the reaction chamber, damaging the reactor. To address these issues, Thio developed the concept of using plasma liners for MIF [10]. In this concept, a series of plasma jets are fired from plasma guns and form a cylindrical or spherical liner. This liner then implodes on a magnetized fusion fuel target and brings it to fusion conditions. The concept as envisaged by Thio is referred to as plasma-jet-driven magneto-inertial fusion (PJMIF), Fig. 1. Formation of a spherically imploding plasma liner via merging plasma jets is now being pursued on the plasma liner experiment (PLX) at Los Alamos National Laboratory [11].

To motivate the choice of test cases put forth in this paper, the physical processes of liner formation and implosion are discussed below. Since the immediate objectives of PLX include the study of the scaling of peak ram pressure, defined as

$$p_r = \rho u^2 \qquad (1)$$

Liner uniformity is another important figure of merit for PLX. Accordingly, the scope of this work is limited to physical processes prior to target compression and liner stagnation. First, the plasma jets are formed and accelerated by pulsed plasma guns,
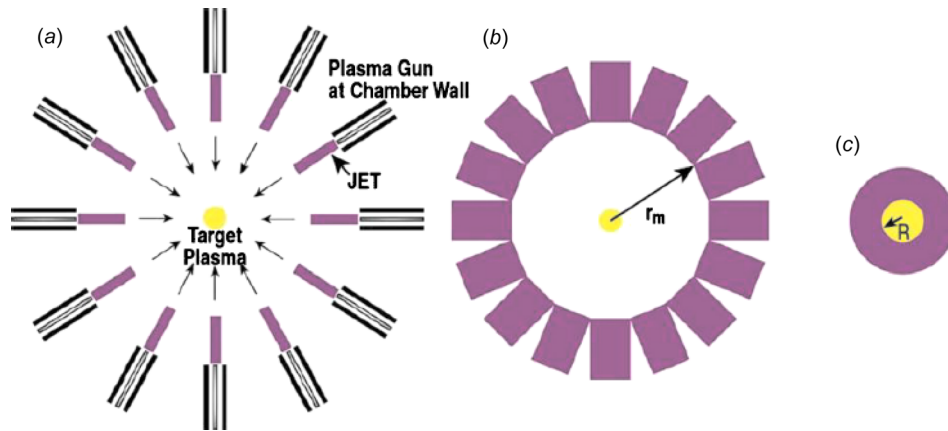
Fig. 1 Spherically symmetric plasma-jet-driven magneto-inertial-fusion concept [12] showing (*a*) plasma jets launched from an array of plasma guns, (*b*) merging of the plasma jets to form a plasma liner, and (*c*) compression of a target by the imploding plasma liner

Fig. 1(*a*). The jets will be fully ionized with a temperature of a few eV, undergoing radiative cooling during propagation through the vacuum. The jets merge at some distance away from the chamber center, forming oblique shock waves at the jet interface. Heat transfer from the post shock layer and the colder jet may occur. Further weaker oblique shocks may occur during subsequent merging of precursor jets formed by the post shock material [13], although the implosion beyond liner formation may be approximately isentropic. During this process, velocity shear may introduce flow structures, which may be dissipated by viscosity. Numerical models often suffer from numerical diffusion and thus these vortical structures and other asymmetries in the flow may be smeared artificially [14].

The stages of liner/target interaction, implosion, stagnation, and rarefaction have been illustrated elsewhere [15] and not duplicated here. However, since the plasma liner has spherical symmetry and will produce a hot spot during liner collapse even in the absence of a target, heat transfer from the hot spot may play an important role in peak ram pressure.

Modeling of PJMIF has been performed since the late 1990's [10] in support of ongoing experiments, which have been supported by both the National Aeronautics and Space Administration (NASA) and the Department of Energy (DOE). These experiments include the ongoing PLX, the objective of which is to merge up to 60 plasma jets with high density and high Mach number to form a spherically imploding plasma liner [11]. Cassibry studied the merging and implosion of twelve plasma jets of deuterium using the MACH2 code. The simulations were two-dimensional and assumed an inviscid flow, with artificial viscosity used to dissipate pressure oscillations behind the shock waves formed by the liner implosion. When a magnetized fusion fuel target was included in the simulations, the magnetic field gradient drove a current along the surface of the target. Ohmic heating further raised the temperature at the surface of the target [16].

Knapp and Kirkpatrick investigated the effect that the implosion velocity of the plasma liner has on the fusion energy gain of PJMIF. Their test cases consisted of one-dimensional implosions of several shells of xenon plasma. Each of these shells had the same inward velocity and different densities. The liner implodes on a shell of deuterium and tritium, and within this shell is a spherical target of deuterium-tritium, with the inner target being warmer and less dense than the outer shell. It was found that reducing the number of layers of xenon gas in the liner reduced the amount of input energy more than it reduced the fusion energy yield. The main conclusion was that simulations yielded cases in which ignition of PJMIF targets produced gains thought to be sufficient for reactors for terrestrial power. These cases were enabled

when electron thermal conduction was suppressed by a magnetized target for liners with implosion velocities of 60 km/s and higher [17].

Cassibry et al. investigated a scaling relationship of the peak pressure for an imploding plasma liner as a function of the plasma jet velocity, the number of jets, the mass of the plasma, the jet Mach number, the radius of the reaction chamber, initial jet diameter, initial jet length, initial arrangement of the jets, the atomic weight of the jet species, and the specific heat ratio [18]. Simulations for this study were conducted using a three-dimensional (3D) smoothed particle hydrodynamic (SPH) code that uses an ideal gas equation of state (EOS) and ignores effects from radiation and thermal conduction losses. Some simulations included adiabatic gas targets that the plasma liner imploded upon. The greatest value for the peak pressure was found to occur at the origin right when the liner implodes on the void. When the jets merge, the radial pressure profile has a sharp leading edge that peaks and decreases.

Santarius used the BUCKY code, a one-dimensional, Lagrangian, radiation-hydrodynamics code to simulate fusion burns in different geometric configurations [19]. The fusion reaction rates for the fuel and the peak pressure were found to occur at about the same time and peaked in value for tenths of a microsecond. The code predicted a peak interface ram pressure of about 14 Mbar. The same simulation was then performed with a two-temperature model, showing greater compression and dwell time. Differences between the one and two-temperature physics models indicate that simulations are very sensitive to the timing of the plasma jets and the parameters defining the thermodynamic state and motion [19].

Kim et al. studied cases for PLX that used a numerical equation of state to model gases that have a high Z for ionization modeling, as well as the deuterium equation of state [13]. Both of these equations of state were used in the FronTier code for one-dimensional spherically symmetric plasma liner simulations. The code was also used to simulate three-dimensional propagation, merging, and implosion of the plasma jets that make up the liner. Simulations for argon and deuterium liners were conducted that incorporated atomic physics. Dissociation energy was found to reduce the liner temperature and increase the Mach number. Before the liner interacts with the target, ionization energy is very small. When the target is compressed by the liner, the front edge of the liner is ionized significantly [13].

Samulyak et al. studied a concept involving a 15 cm thick liner of deuterium that implodes and compresses a target of plasma. A magnetic field was included in the simulation, which acts to suppress the electron and ion heat conduction during the compression

of the target. The theoretical value of the deconfinement time was calculated to be 100 ns, whereas the simulations found the deconfinement time to be about 220 ns. The fusion fuel burnup fraction was found to be 6.67×10^{-4}, much lower than the theoretical prediction of 0.011. The fusion gain was calculated to be 0.012, which was 10.8 times lower than the predicted value. This difference can be attributed to the liner failing to compress the target to the radius of 0.5 cm that was predicted in the theoretical model [12]. PJMIF configurations that are more favorable with respect to energy gain have much lower input energies than those studied by Samulyak [12].

Awe et al. investigated using a one-dimensional radiation hydrodynamic simulation to study the scaling of the stagnation pressure after the plasma has undergone a shock and the useful lifetime of the plasma liner [20]. It was found that centimeter and microsecond scale plasmas can generate peak pressures of 1 Mbar with several hundred kilo Joule of kinetic energy in an imploding spherical liner. Radiation and thermal transport were shown to prevent nonphysical plasma temperatures at the origin, which otherwise limit liner convergence [20]. Davis et al. added a more detailed EOS model to the Awe study, investigating how the new model affected factors such as the liner stagnation pressure, stagnation time, implosion trajectory, and minimum radius achieved for spherically symmetric plasma liner implosions [21]. This study used a local thermodynamic equilibrium and non-local thermodynamic equilibrium equation of state models, both of which yielded similar stagnation pressures that were lower than the stagnation pressures reported in the Awe study. This can be attributed to ionization and electron excitation acting as an energy sink, which reduces the compression of the liner [21].

Specific test cases have been reported for PJMIF codes before, as was done in several of the papers cited above. This includes Noh shock tests reported by Cassibry et al. [22] and implosions of plasma liners and plasma target compressions reported by Samulyak et al. [12]. To the authors' knowledge, no one has examined tests of equations of state and transport physics that incorporate tabular lookup for heat conduction, radiation, physical viscosity, and numerical diffusion in the context of plasma jet driven magneto-inertial fusion.

Smooth particle hydrodynamics is an advanced numerical algorithm that has potential for application in MIF. One of the primary reasons for this potential is that MIF concepts involve vacuum/plasma interfaces in which the plasma shape compresses and expands by orders of magnitude, and internally there are stratified layers in which mixing and instabilities can disrupt or eliminate the yield of the fuel pellet. Since SPH is naturally adaptive and particles can be tracked for all times [23,24], the compression/expansion and mixing processes can potentially be resolved very accurately due to the Lagrangian nature of the SPH method. There are a number of open problems in MIF that have to be solved, and no one code can solve them all. The primary motivation behind the development of SPFMax is to help address some of these problems. The objective in developing this code is to be able to simulate experiments of relevance and produce results that are within 10% of experimental measurements without requiring significant computational resources. Keeping the code relatively small and functional on a laptop or single workstation has allowed for the implementation of a number of advanced physics and enabled a high number of runs without difficulty in management of the numerical output. The current physics package includes shock capturing, tabular equations of state, ionization, heat conduction, phase change tracking, particle tracking, real viscosity, separate ion and electron energy equations, thermal electron/ion equilibrium, nonlocal multigroup radiation emission and absorption, fusion and fission reaction rates and nonlocal deposition of fusion and fission products, fission reactivity, and electromagnetic fields. A number of on-the-fly diagnostics have been added to facilitate comparisons with experimental data, including static and Lagrangian probes for

tracking history of the properties, interferometry, spectrometery, shadowgraph, and schlieren imaging.

Another major motivation for the development of SPFMax is the PLX-α project, which seeks to demonstrate the formation of a spherically imploding plasma liner by merging supersonic plasma jets. Simulating this with 3D hydrodynamics codes is crucial for determining nonuniformities that arise from the liner/target interface, which require 3D simulations and to guide development of 4π experiments, with simulations accurate to 10% or better for predicting PLX-α experimental data [25].

This paper presents a test suite to support using SPFMax for 3D modeling for PJMIF. Simulations were conducted that incorporated the physics of radiation cooling, heat transfer, oblique shock capturing, angular momentum conservation, and viscosity [26,27]. The physics and numerical approach of this new SPH code are given here as well, and the code is used to perform all numerical simulations presented in this paper. Section 2 describes the numerical method of SPH and the equations that the code solves. The test cases and results are described in Secs. 3–8. In the discussion of the test cases, the accuracy is measured with the L^2 norm, and the objective in each test is to achieve 10% or better accuracy, consistent with the long-term, ongoing objective of achieving 10% accuracy with experimental results as data become available. Conclusions are presented in Sec. 9.

2 Smooth Particle Hydrodynamics Model

Smooth particle hydrodynamics is a meshless Lagrangian method that simulates fluid flows by dividing a fluid into a set of particles and using a summation interpolant function to calculate the properties and gradients for each of these particles [23,24]. A kernel function is then used to calculate the properties for each of these particles by adding up the properties of the particles that lie within the kernel. The properties assigned to a specific particle are determined based on the density and proximity of other nearby particles [27–29]. Informally, SPH is a method for (1) interpolation of scattered data within a region of compact support, a distance of frequently twice the interparticle spacing and (2) calculation of first and higher order derivatives of the properties of scattered data.

For the kernel approximation, an integral interpolant can be used to obtain the value for any property in a fluid, and is defined as [23]

$$A(r) = \int A(r')\delta(r - r')dr' \qquad (2)$$

The delta function is given by [23]

$$\delta(r - r') = \begin{cases} 1 & r = r' \\ 0 & r \neq r' \end{cases} \qquad (3)$$

By replacing the delta function with a smoothing function, the kernel approximation can be expressed as

$$A(r) = \int A(r')W(r - r', h)dr' \qquad (4)$$

The smoothing function is required to meet several constraints. The first is the normalization condition, which can be expressed as

$$\int W(r - r', h)dr' = 1 \qquad (5)$$

The second constraint is the delta function property in the limit as h approaches 0, given by

$$\lim_{h \to 0} W(r - r', h) = \delta(r - r') \tag{6}$$

The third constraint is the compact support condition, and is given by

$$W(r - r', h) = 0 \ \text{when} \ |r - r'| > \kappa h \tag{7}$$

After the kernel function has been applied, the particle approximation is utilized. In the particle approximation, the system is represented by a finite number of particles, with each particle characterized by mass and location. The continuous integral representations in the kernel approximation are converted to discretized forms of summation over all of the particles that lie within the support domain. This allows the integral interpolant to be approximated with a summation interpolant given by

$$A(r) = \sum_b m_b \frac{A_b}{\rho_b} W(r - r_b, h) \tag{8}$$

The spatial gradient for this quantity can be computed using the equation summation

$$\nabla A(r) = \sum_b m_b \frac{A_b}{\rho_b} \nabla W(r - r_b, h) \tag{9}$$

The single fluid equations of motion are solved in SPFMax. Conservation of mass is given by

$$\frac{\partial \rho}{\partial t} + \nabla \cdot (\rho u) = 0 \tag{10}$$

In our code, conservation of mass is solved exactly by replacing the continuity equation above with

$$\rho_a = \sum_b m_b W_b \tag{11}$$

The momentum equation is given by

$$\frac{d\boldsymbol{u}}{dt} = -\frac{1}{\rho} \nabla p + -\frac{1}{\rho} \nabla \cdot \tau + \nabla \Pi \tag{12}$$

The bulk viscosity coefficient is defined as

$$\lambda = -\frac{2}{3} \mu \tag{13}$$

The single temperature energy equation is given by

$$|A - \xi| < C n^{-p} \tag{14}$$

PROPACEOS is used to generate the equations of state and opacity data for the fluids in the SPH code, as well as specific internal energies and pressures [28]. Alternatively, an ideal gas model can be used as is done in some of the test cases in this paper.

In SPH, the first derivative for u with respect to x can be calculated as

$$\frac{\partial u}{\partial x} = \sum_b V_b u_{ab} \nabla_x W_{ab} \tag{15}$$

The second derivative can then be defined as

$$\frac{\partial^2 u}{\partial y \partial x} = \sum_b V_b \left(\frac{\partial u}{\partial x}\right)_b \nabla_y W_{ab} \tag{16}$$

Thus, the code stores first-order derivatives as particle properties, which are needed to calculate second-order derivatives [29]. This is necessary for the three spatial derivatives of each of the three velocity components [30,31], as well as the scalar temperature for the heat conduction equation [32]. It is worth noting that this is not a common way to evaluate second-order derivatives in SPH. Most often, SPH methods use a summation interpolant with the first-order gradient of the kernel with an estimate of the derivative using a finite difference-like operation of the particle and its neighbor properties. An example of this is the artificial viscosity term described in the review paper by Monaghan [24]. The typical approach is taken because summation interpolants using the second derivative of the kernel function are susceptible to error at low particle resolution [33]. More recently, Fatehi et al. investigated all three of these methods as well as proposed a fourth method with third-order accuracy. The new method showed improvement in convergence, although the implementation is more complex and requires solving a system of linear equations to obtain normalization constants for the summation [29]. Since no method is perfect, the approach used in this study was selected because it was found to offer simplicity and accuracy for the complex problems that the SPH code will be used to explore. In addition, the problem of nonphysical oscillations, which can occur in this approach, can be made acceptably small with sufficient particle resolution.

A sequence of simulations converges to a value of ξ with order p if it meets the following criteria:

$$|A - \xi| < C n^{-p} \tag{17}$$

in which C is a constant and n is the number of grid points. For code verification, ξ is equal to zero, since the error should approach zero as the resolution increases.

The L^2 norm is a popular norm in the fields of science and engineering that can be used to measure accuracy. Using density as an example, the L^2 norm can be calculated using the following equation:

$$L_\rho^2 = \sqrt{\frac{(\rho - \rho_{\text{exact}})^2}{n}} \tag{18}$$

The L^2 norm provides a global average error. This method is used to measure the error for density, temperature, and pressure at different resolutions. A higher resolution generates more particles, which in turn should provide a more accurate solution. To perform an L^2 analysis, it is necessary to perform simulations of problems in SPH that have analytical solutions. As mentioned in the introduction, the primary objective of this study was to incorporate physical viscosity, oblique shock capturing, radiative cooling, and heat conduction into the SPH code and perform verification tests against problems relevant to plasma liner formation for the PJMIF concept. Each of the test cases required an analytical solution in order to assess the accuracy of code in simulating these different physics. The simulated problems consisted of optically thin radiation cooling, thermal conduction, Couette flow, the Gresho vortex, oblique shock, and the Taylor-Green vortex. The descriptions and results for each of these problems is provided in Secs. 4–8.

3 Optically Thin Radiation Cooling

The cooling rate for single group radiation in the optically thin limit is given by (see Planck's law in Ref. [34])

$$\frac{de}{dt} = 4\sigma T_e^4 \chi_{\text{Planck}} \qquad (19)$$

If it is assumed that the electron and ion temperatures are equal $(T_e = T_i \equiv T)$, then the specific internal energy for the system is $e = C_v T$. The value for C_v is given by

$$C_v = \frac{\bar{R}(1+Z)}{\text{AW}(\gamma - 1)} \qquad (20)$$

where Z is the charge state of the plasma, AW is the atomic weight, $\bar{R}$ is the universal gas constant, and γ is the specific heat ratio. Thus, in terms of temperature for a calorically perfect gas, the rate of change in temperature becomes

$$\left(\frac{dT}{dt}\right)_{\text{rad}} = 4\sigma T^4 \chi_{\text{Planck}} \frac{\text{AW}(\gamma - 1)}{\bar{R}(1+Z)} \qquad (21)$$

The problem examined consists of a region of argon plasma with a constant ion density of 10^{22} m^{-3} and an initial temperature of 2 eV. Two simulations were run, with one using Eq. (18) in which the parameters opacity, specific heat ratio, and charge state were fixed, consistent with the 2 eV temperature and ion density. The other simulation used Eq. (20), with the parameters and temperature of the plasma being interpolated from an equation of state table during the numerical integration as a function of e and ρ.

Temperature is plotted versus time in Fig. 2, for both the ideal case of constant opacity and calorically perfect gas and the tabular case in which all properties are a function of ρ and e. In both simulations, cooling occurs rapidly in the first 2 μs, followed by a more gradual cooling in the remaining 18 μs. The solutions were determined by integration using the ordinary differential equation 45 solver, a MATLAB algorithm that utilizes a Runge Kutta 45 numerical integration scheme [35]. The results from the SPH plot are shown for the same two cases as points, which fall on top of the exact results, indicating that the radiation model is implemented properly, and that the table lookup in the SPH model is performing consistently with the exact numerical.

4 Thermal Conduction

As the plasma jets merge, shock heating and compressional work will heat the exterior of the jets and then thermal transport will contribute to heating the interior of the jets. To verify that SPFMax can capture heat transfer, the heat conduction problem is solved using cylindrical symmetry, where the outer radial boundary is set to a constant temperature that is higher than the interior temperature.
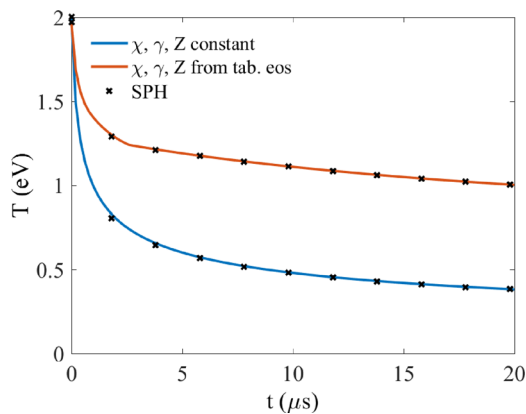
A model for this problem can be derived from the form of the heat equation as given by

$$\rho C_v \frac{\partial T}{\partial t} = \nabla \cdot (k \nabla T) \qquad (22)$$

This partial differential equation can be solved exactly under the assumption of constant coefficients for various boundary conditions in planar, cylindrical, and spherical geometries in 1D, 2D, and 3D. This is accomplished by using separation of variables on a nondimensionalized form of the equation assuming periodic boundary conditions, and infinite boundary condition solutions can be found as well. While solutions can be found in numerous textbooks, the authors found the report by Vansant particularly useful [36]. For constant, uniform temperature T_0 at r_0 and initially uniform temperature T_i, the solution gives
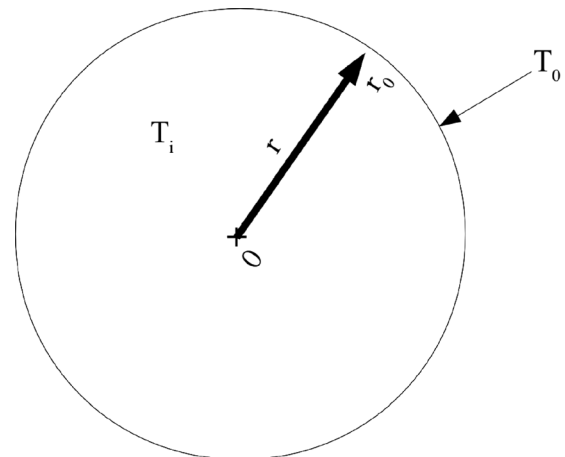
$$T(r,t) = T_0 + 2(T_i - T_0)\sum_{n=1}^{\infty} \frac{1}{\lambda_n} e^{-\lambda_n F_o(t)} \frac{J_0(\lambda_n R)}{J_1(\lambda_n)} \qquad (23)$$

The test case is illustrated in Fig. 3.

The problem investigated is one of a cylinder of argon plasma with constant ion density of 10^{22} m^3 and 1 eV initial temperature. The boundary is set to 10 eV with 2.5 cm initial radius. The equation of state and transport properties are found using the PROPACEOS [28] tabular equation of state at an intermediate temperature of 3 eV, with $k = 8.6609$ W/m K, AW $= 39.948$ kg/k mol, $Z = 2.5587$, and $\gamma = 1.1166$. The series solution is truncated with the first 100,000 terms, evaluated at each point in the spatial direction from $r = 0$ to 2.5 cm, and at times from $t = 0$ to 100 μs. Figure 4 shows a plot of the temperature versus the radius of the cylinder at fixed times for the exact and numerical solutions. The SPH results were obtained using a line slice through the cylinder located at $z = 5$, $y = 0$, and $x = -2.5$:2.5 cm.

Temperature increases with radius, with a minimum value located at $r = 0$ cm, and a maximum value of 10 eV at the boundary. The temperature profiles change as time progresses to the Fourier time as given by [36]

$$t = F_0 \frac{\rho C_v r_0^2}{k} \qquad (24)$$

Fig. 2 Plasma temperature as a function of time. Solid lines indicate exact numerical solution and data points are SPFMax results.

Fig. 3 Initial conditions for heat conduction problem with cylindrical symmetry

For this problem, the Fourier time is on the order of ∼64 μs. After this time, the temperature curve becomes constant at 10 eV, as seen by the exact numerical solution in Fig. 4.

The SPH results can be seen to be in general agreement with the analytical solution, with the difference between the SPH results approaching the analytical solution as time progresses. This can be further seen in Fig. 5, which provides an L^2 norm for the temperature versus the number of particles at three fixed times during the simulation run.

From this figure, it can be seen that the SPH results become more accurate as time progresses. This applies for the convergence rates as well. The convergence rate for the results at 10, 30, and 100 μs are $N^{-0.17}$, $N^{-0.28}$, and $N^{-0.47}$, respectively. This is somewhat lower than convergence rates reported by other SPH studies [37]. The relatively high inaccuracies (20–30%) are found at early times when temperature gradients are most severe, but for sufficiently high particle resolution and equilibration time, the accuracy improves to well within 10%.

As the spherical liner converges and stagnates, a hot spot is formed in which heat conduction transfers energy radially outward. Because of this, it was desired to conduct an additional thermal conduction test case for a spherical geometry.

For a sphere with steady surface temperature T_0 and uniform initial temperature T_i, the transient solution for temperature in the sphere as a function of time and radius is given by [36]

$$T(t,r) = (T_i - T_0) \left\{ 1 - \frac{1}{(r/r_0)} \sum_{n=1}^{\infty} \left[\mathrm{erfc}\left(\frac{2n - 1 - (r/r_0)}{2\sqrt{F_o(t)}} \right) \right. \right.$$
$$\left. \left. - \mathrm{erfc}\left(\frac{2n - 1 + (r/r_0)}{2\sqrt{F_o(t)}} \right) \right] \right\} + T_0 \qquad (25)$$
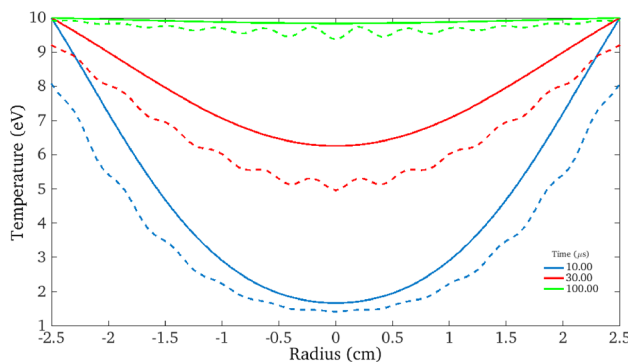
where the Fourier number is given by

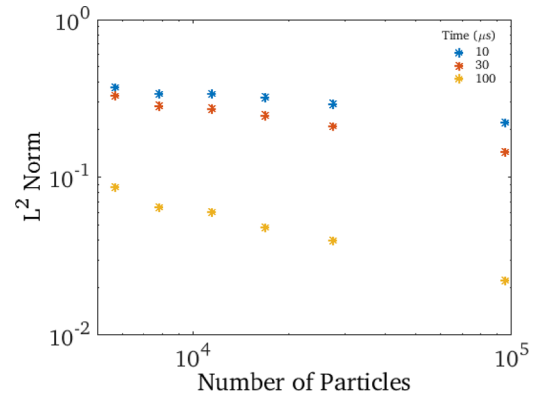$$F_o(t) = \frac{\alpha t}{r_0^2} \qquad (26)$$

The diffusivity is given by

$$\alpha = \frac{k}{\rho C_v} \qquad (27)$$

Figure 6 shows a cutaway of the initial thermal condition for the SPH simulation using spherical geometry. This figure illustrates the lower uniform temperature along the surface of the sphere and the higher initial temperature throughout the entire inner volume of the sphere.

Fig. 5 Temperature L^2 norm for heat conduction problem in cylindrical symmetry

A comparison of the SPH solution with the exact solution for the spherical geometry as a function of time is shown in Fig. 7. The figure shows the temperature profile at five different points in time. The solid lines are the values for the analytical solution and the dotted lines are the values obtained in SPFMax. In general, the code provides more accurate results closer to the center of the geometry. The accuracy of the SPFMax results is also seen to get more accurate as the simulation progresses in time.

An L^2 analysis for the temperature is given in Fig. 8. This shows the L^2 norm for temperature converging at a nearly constant linear slope as time progresses. The error is ∼6% for most of the simulation.
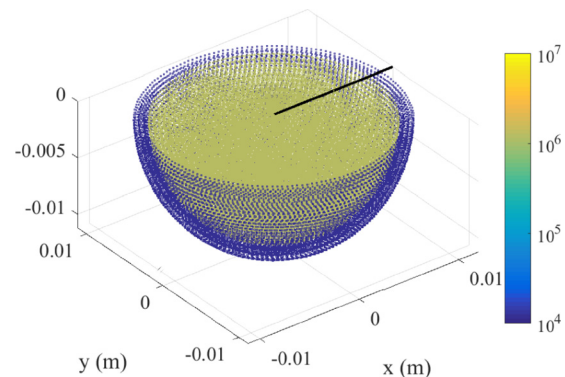
The decrease in the L^2 norm can be attributed to the temperature profile becoming more uniform during the simulation run.
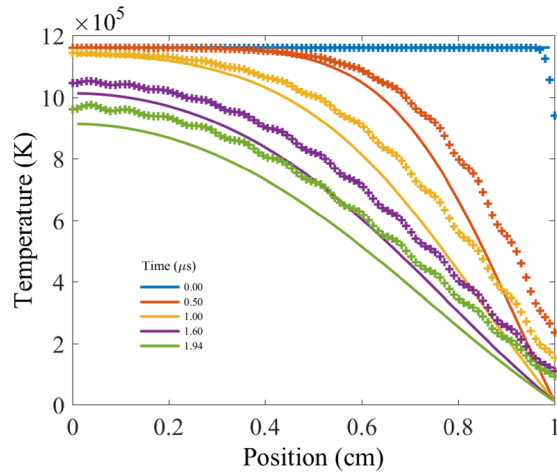
5 Couette Flow

Couette flow consists of a viscous fluid that is contained between two infinite parallel plates. The plates are separated by a constant distance, the upper plate moves at constant velocity relative to the bottom plate. The flow is incompressible, and the thermal conduction and dynamic viscosity of the fluid are assumed to be constant. When the no-slip condition is applied to this problem, there is no relative motion between the fluid and the plate [38]. The exact solution for the fluid flow velocity between the plates can then be written as

$$u(y) = u_e \frac{y}{D} \qquad (28)$$

An illustration of the velocity profile is shown in Fig. 9. The simulation was two-dimensional and used geometry that was one particle thick in the y direction. The Couette flow problem assumes an

Fig. 4 Temperature profile at different times for heat conduction problem with cylindrical symmetry. Solid lines indicate exact numerical solution, and dotted lines are SPFMax results.

**Fig. 6 Initial condition for heat conduction problem in spherical geometry**

Fig. 7 Temperature slice comparison of SPH solution with exact numerical solution for heat conduction problem with spherical symmetry. Solid lines indicate exact numerical solution and dotted lines are SPFMax results.
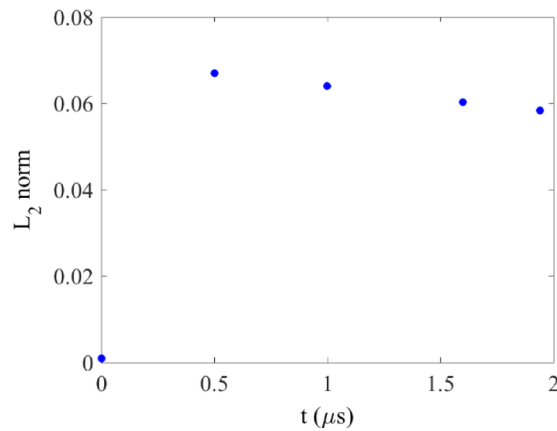

Fig. 8 L^2 norm at different times for heat conduction problem with spherical symmetry

infinitely long geometry, making it difficult to simulate in SPH. To address this, periodic boundary conditions were implemented by using an algorithm that transfers particles that move beyond the maximum geometry position in the x direction to the minimum
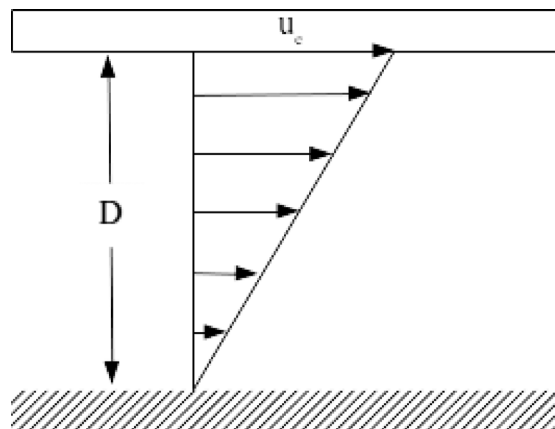
Fig. 9 Incompressible Couette flow velocity profile
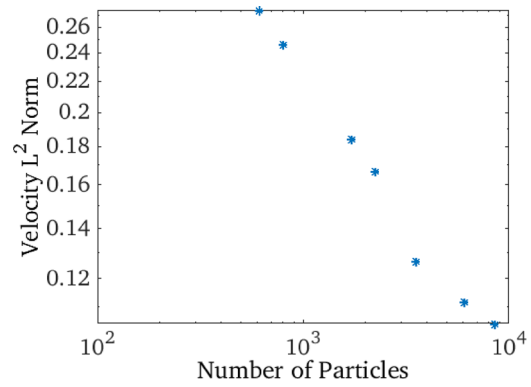
Fig. 10 L^2 norm for Couette flow velocity

position in the x direction, and vice versa. This allows for a finite geometry to be used in the simulation of Couette flow.

Numerous simulations with different particle numbers were run in order to conduct an L^2 norm analysis. The results for the L^2 norm are presented in Fig. 10. The convergence rate is on the order of $N^{-0.38}$. This shows that SPFMax is able to incorporate viscous effects in the Navier–Stokes equations with a reasonable level of accuracy, and is consistent with the order of accuracy reported in other SPH studies [14]. More importantly, with only 10^4 particles, 10% accuracy is achieved.
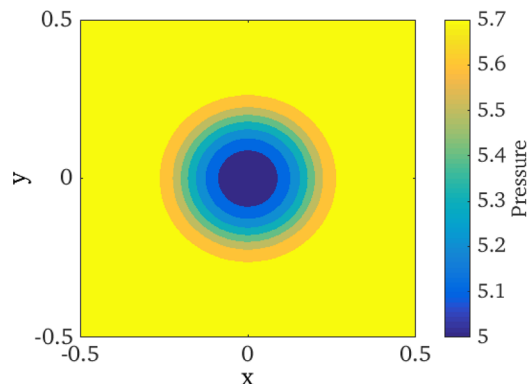
6 Gresho Vortex

The Gresho vortex is an inviscid, time-independent, incompressible problem that consists of a rotating vortex. The azimuthal velocity is dependent only on the radius, and the centrifugal force is balanced by the pressure gradient [38]. The Gresho vortex allows for the testing of a numerical code's preservation of symmetry and conservation of angular momentum as a function of time.

The azimuthal velocity of the vortex is given by

$$u_\phi(r) = \begin{cases} 5r, & 0 \leq r \leq 0.2 \\ 2 - 5r, & 0.2 \leq r \leq 0.4 \\ 0, & 0.4 \leq r \end{cases} \quad (29)$$

The pressure in arbitrary units is given by Eq. (30) and is illustrated as a contour plot in Fig. 11. As shown, the pressure is lowest in the center of the vortex where the azimuthal momentum is relatively high, which is balanced by higher pressure surrounding the vortex
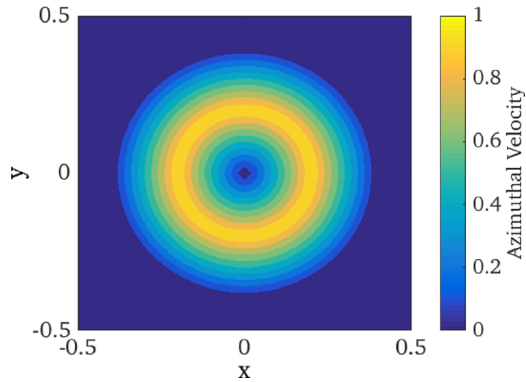

Fig. 11 Gresho vortex pressure contour

Fig. 12 Gresho vortex azimuthal velocity contour

Fig. 14 L^2 norm for Gresho vortex pressure

$$p(r) = \begin{cases} 5 + \dfrac{25}{2}r^2, & 0 \le r \le 0.2 \\[2mm] 9 - 4\ln 0.2 + \dfrac{25}{2}r^2 - 20r + 4\ln r, & 0.2 \le r \le 0.4 \\[2mm] 3 + 4\ln 2, & 0.4 \le r \end{cases} \tag{30}$$

Figure 12 shows contours for the azimuthal velocity of this specific Gresho vortex. This figure shows that the azimuthal velocity is 0 at the center of the vortex, and increases linearly until it reaches a maximum value at $r = 0.2$. The azimuthal velocity then decreases linearly to 0 once $r = 0.4$.

Numerous simulations of this vortex were conducted with SPFMax, each one with a greater number of particles. Figure 13 shows the Gresho vortex simulation in SPFMax. While the Gresho vortex is a time-independent solution, simulations of the vortex inevitably degrade from the analytical solution as time progresses due to factors such as numerical diffusion [14]. Ways to mitigate this in the future include using a Balsara switch [40] to suppress artificial viscosity in the presence of shear to permit inviscid rotational structures in the fluid.

A total simulation time of 1.25664 s was used for these test cases. This time was selected to allow the fastest rotating fluid in the vortex to undergo one complete rotation. The pressure and angular velocity for each of these simulations were then compared to the profiles given by Eqs. (27) and (28), allowing for an L^2 norm to be obtained for both of these parameters. The results for the L^2 norm are presented in the following two figures. The results for the L^2 norm for the Gresho vortex pressure and azimuthal velocity are presented in Fig. 14 and Fig. 15, respectively.
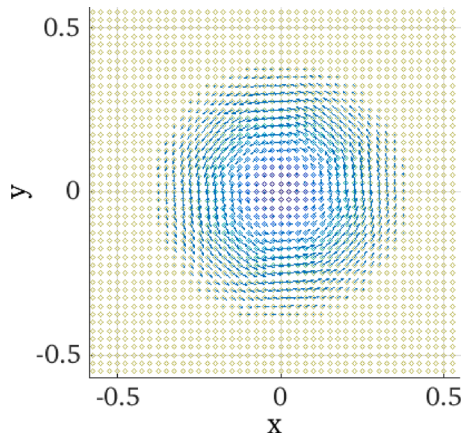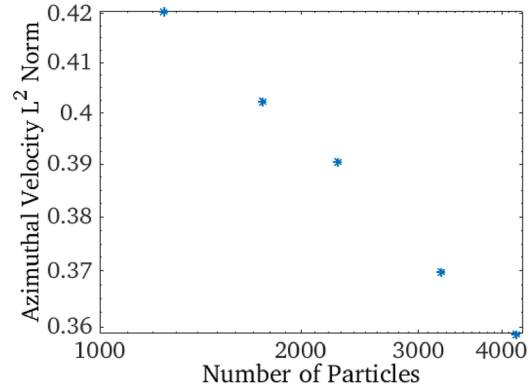

Fig. 15 L^2 norm for Gresho vortex azimuthal velocity

The convergence rate of the Gresho vortex pressure is on the order of $N^{-0.13}$, while the convergence rate for the azimuthal velocity is on the order of $N^{-0.1}$. This is somewhat lower than convergence rates that have been reported by other SPH codes [37]. However, it should be noted that most SPH simulations of the Gresho vortex have only evolved the vortex to a time of $t = 1$ s, which is less than one complete rotation of the fastest moving gas particles in the vortex [37]. In comparison, this study simulated one complete rotation of the fastest moving gas particles.

Many SPH codes have been reported to have extreme difficulty in accurately simulating the Gresho vortex. This is due to particle shear motion requiring constant recalculation of the effective particle volume. The changing of the particle volume leads to noise in the volumetric and velocity fields. Artificial viscosity can be used to dampen the velocity noise at the expense of diffusing the vortex [14]. The viscous dissipation resulting from particle motion can also be misinterpreted by the code as the presence of shocks. Better shock capturing methods may improve the accuracy of simulating problems like the Gresho vortex, and will be the subject of future work. For this particular problem, MIF flows involving strong mixing, such as late time beyond the onset of Rayleigh Taylor or Richtmyer–Meshkov instabilities.

7 Oblique Shock

In the plasma liner experiment, supersonic plasma jets will merge with half angle between jets of 10–20 deg, and it is anticipated that this will produce oblique shocks since the jets will be deflected in the direction of the jet to jet interfacial plane. Experiments on oblique merging of two supersonic jets were conducted by Merritt et al. for PLX at Los Alamos National Laboratory. These experiments measured the stagnation layer formed by the

Fig. 13 SPFMax Gresho vortex simulation, with vectors indicating direction of flow

two obliquely merging supersonic jets and characterized the time evolution of the oblique shock merging [41,42].

The solution to the so-called jump conditions across a shock can be found in numerous compressible flow textbooks [43]. In the ideal case of a stationary ramp, the shock angle β, merging half angle θ, and the incoming jet Mach number are related by the so-called θ-β-M relation

$$\tan\theta = 2\cot\beta \left[\frac{M_1^2 \sin^2\beta - i}{M_1^2(\gamma + \cos 2\beta) + 2} \right] \qquad (31)$$

The jump conditions across the oblique shock are identical in form to those of a normal shock, with Mach number replaced with the normal component of the Mach number orthogonal to the shock. The normal component of Mach number is

$$M_{n1} = M_1 \sin\beta \qquad (32)$$

The shock relations for density and pressure are

$$\frac{\rho_2}{\rho_1} = \frac{(\gamma + 1)M_{n1}^2}{(\gamma - 1)M_{n1}^2 + 2} \qquad (33)$$

$$\frac{p_2}{p_1} = 1 + \frac{2\gamma}{\gamma + 1}\left(M_{n1}^2 - 1\right) \qquad (34)$$

The normal component of the Mach number downstream from the shock is

$$M_{n2}^2 = \frac{M_{n1}^2 + \left[\dfrac{2}{\gamma - 1}\right]}{\left[\dfrac{2\gamma}{\gamma - 1}\right]M_{n1}^2 - 1} \qquad (35)$$

The actual Mach number downstream of the shock is determined with

$$M_{n2} = M_2 \sin(\beta - \theta) \qquad (36)$$

Using the ideal gas law, the temperature is calculated with

$$\frac{T_2}{T_1} = \frac{p_2}{p_1}\frac{\rho_1}{\rho_2} \qquad (37)$$

A test case is chosen with initial conditions of two jets with conditions comparable to anticipated PLX jet parameters, with velocity of 40 km/s, 10 deg merging half angle, argon gas with $\gamma = 1.3$, initial mass density of 1.33×10^{-3} kg/m^3, and initial temperature of 16,247 K (1.4 eV), which corresponds to an initial Mach number of 19.1. Using the oblique shock relations, the exact solution for a stationary ramp gives a shock angle of 12.28 deg. This implies that the merge layer between the jets should grow at the jet interface with a 2 deg shape ($\sim$12 deg shock angle minus 10 deg half angle), a post shock density of 7.24×10^{-3} kg/m^3, a post shock Mach number of 10.13, and post shock temperature of 55,054 K (4.74 eV). It should be noted that the "exact" solution is not a perfect representation of the merging of two discrete jets, as the leading and trailing edges of the jets provide a 2D relieving effect, which is difficult to quantify. A scatter plot is presented in Fig. 16 showing the jets at 0, 5, and 10 μs with the particle color scaled to temperature in Kelvin. The shock is shown to form at 5 μs at the interface between the jets and is well defined at 10 μs. Thermal expansion at the edges of the jets is visible at 10 μs. The simulation is performed in the x–z plane with motion in the y-direction prohibited to allow comparison with the exact solution to the oblique shock, which is a 2D solution.

In Table 1, results are given for the post shock density, temperature, shock angle, and Mach number for three resolutions of

(a)

(b)

(c)
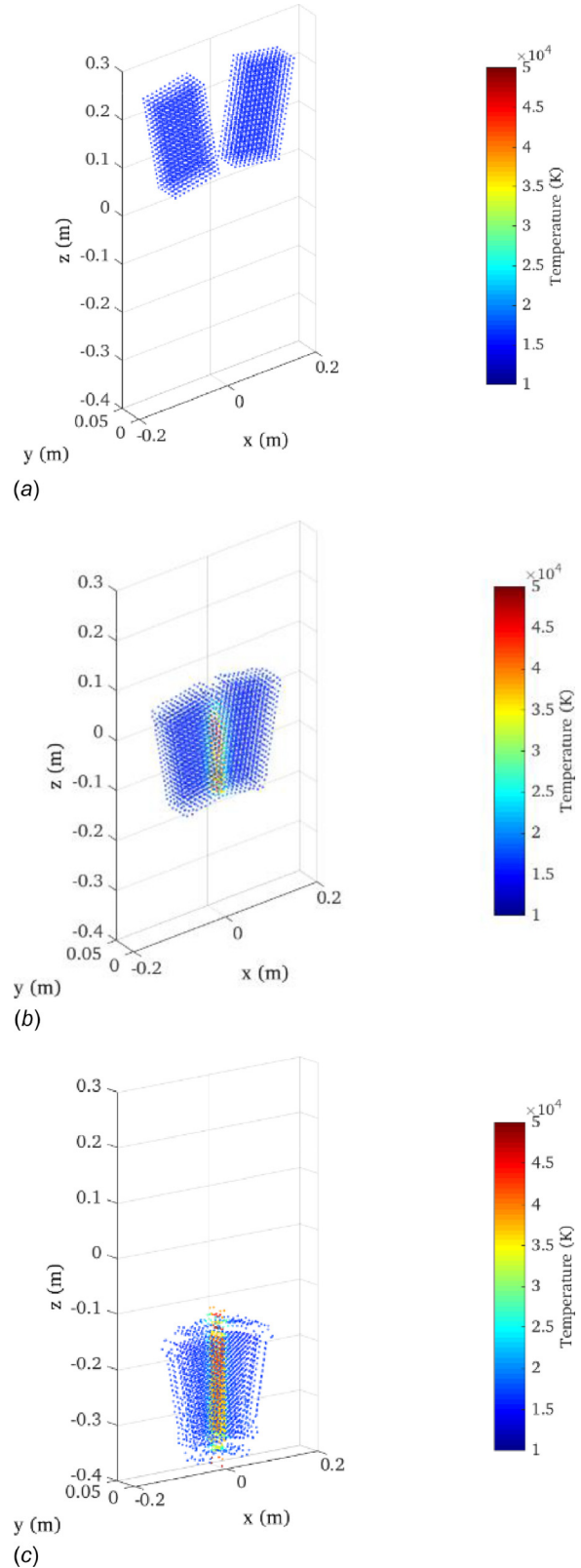
Fig. 16 Scatter plot of jet temperature for the oblique shock test at 0, 5, and 10 μs. The jets intersect with a merging half angle of 10 deg, with the shock visible at the jet–jet interface.

particles. To obtain numerical results, line slices were taken through the numerical output. The shock angle was obtained by generating line slices through the output at three different x_s and z_s locations in the post shock region. The z_s positions were

Table 1 Summary of oblique shock test cases with particle numbers varying from 1386 to 33,728 particles per jet. The exact solution for a stationary ramp gives 12.23 deg shock angle, and post shock density, temperature, and Mach number of 7.24×10^{-3} kg/m³, 55,054 K, and 10.13, respectively.

Case	Number of particles per jet	z_s (m)	ρ_s (kg/m³)	x_s (m)	T_s (K)	β (degrees)	M_s
1	1386	−0.150	0.00526	0.0924	41,070	—	11.82
1	1386	−0.185	0.00693	0.0933	40,100	8.53	11.97
1	1386	−0.22	0.00832	0.093	39,620	10.49	12.02
2	9471	−0.150	0.00781	0.0961	46,720	—	11.04
2	9471	−0.185	0.01049	0.0959	45,960	10.33	11.11
2	9471	−0.220	0.01165	0.0949	45,880	11.64	11.09
3	33,728	−0.150	0.01052	0.0959	47,040	—	10.92
3	33,728	−0.185	0.01114	0.0957	49,740	10.30	10.77
3	33,728	−0.220	0.00824	0.0940	50,880	12.67	10.56

examined at a simulation time of 7.5 μs, with the z_s values set to −0.15, −0.185, and −0.22 m.

An L^2 norm analysis was done for these results in order to find the convergence of the postshock solutions. The convergence rates for the postshock density, temperature, and shock angle are $N^{-0.46}$, $N^{-0.9}$, and $N^{-0.98}$, respectively. At low resolution, the shock temperature is ∼27% less than the exact solution, while in the shock layer, the density spread is from −27% to +15% of the exact result. The shock angle is as much as 30% low of the exact solution. Improvement is seen as the particle number increases to 33,728 for temperature, in which all measurements were within 10% of the exact solution. Density was found to be consistently higher in all cases, ranging from as high as 53% to as low as 14% of the exact solution. The Mach number was within 10% at all measurements. The variation in density is consistent with variation in line integrated interferometry comparisons with experimental data in early six jet conical simulations [25], whereas Mach number from simulations has been found to fall within the scatter of the data [44]. The discrepancy in density and slight underprediction in temperature for the high resolution case suggests that the artificial viscosity is not decelerating the particles sufficiently and needs to be explored further. As with the Gresho vortex test case, a Balsara switch or other means of screening shear while properly decelerating particles to prevent interpenetration beyond the interparticle spacing h is a challenge to be explored in future work.

8 Taylor-Green Vortex

The Taylor-Green vortex is an incompressible, viscous, time-dependent decaying vortex that has an exact closed-form solution. The problem consists of a cubical volume of fluid with an initially smooth vorticity distribution. As time progresses, the vortices interact until they break down into turbulence, which dissipates the energy in the fluid and eventually brings it to rest. This problem has been used to study energy dissipation, vortex dynamics, and turbulent decay [45,46]. The problem has been used in other SPH codes to assess the effect of incorporating viscosity effects in the code's utilization [47].

The velocity field is given by

$$u = \sin x \cos y \, F(t) \tag{38}$$

$$v = -\cos x \sin y \, F(t) \tag{39}$$

in which

$$F(t) = e^{-2\nu t} \tag{40}$$

The pressure is given by

$$p = \frac{\rho}{4}\left(\cos(2x) + \cos(2y)\right)F^2(t) \tag{41}$$

An example problem that was investigated for this study had a dynamic viscosity of 2 Pa·s, a density of 50 kg/m³, and was simulated for a total of 5 s. Figure 17 shows the velocity vectors of this vortex at 0 s and 5 s. The pressure contour at both 0 s and 5 s is shown in Fig. 18. After 5 s have passed, the velocity of the vortex has decayed dramatically and the pressure has decreased significantly due to the slowing of the vortex.

After a sufficient number of simulations were conducted, an L^2 norm analysis of the temperature and x/y velocity components was performed and the results are shown in Figs. 19(a) and 19(b). The convergence rates for the Taylor-Green temperature, v_x, and v_y are $N^{-0.1}$, $N^{-0.15}$, and $N^{-0.11}$, respectively. This again is consistent with the order of consistency reported by other SPH codes
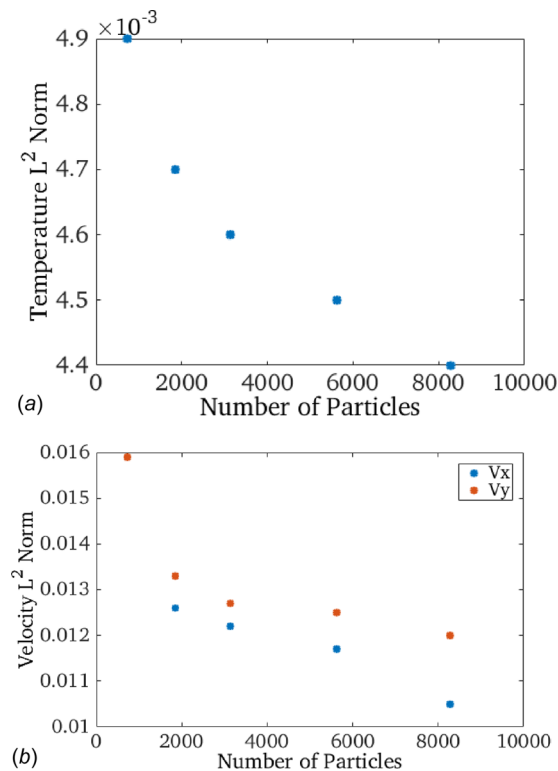

(a)

(b)
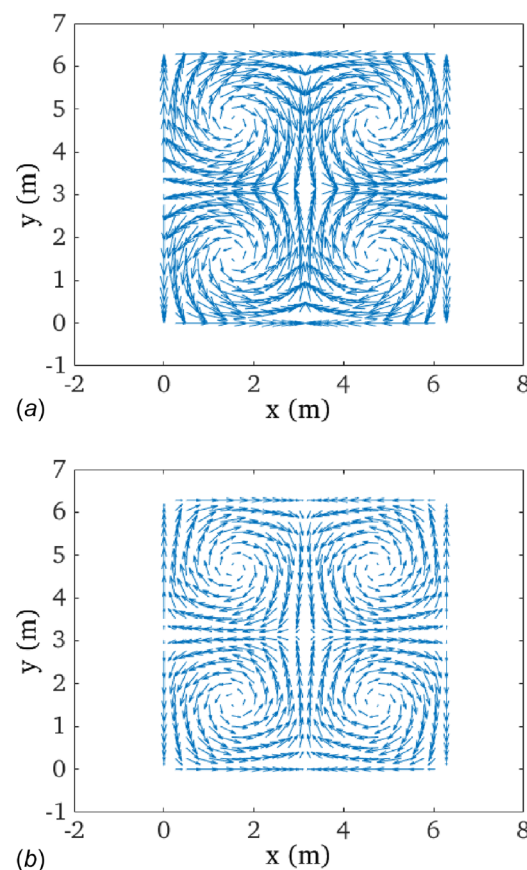
Fig. 17 Taylor-Green Vortex velocity vectors at (a) 0 s and (b) 5 s
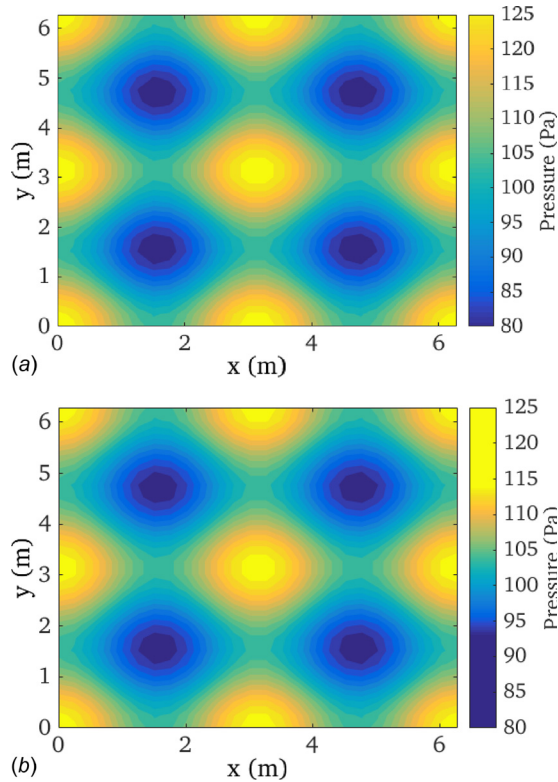
Fig. 18 Taylor-Green Vortex pressure contour at (*a*) 0 s and (*b*) 5 s

in the literature [14], and as can be seen the results are well within 10% accuracy for temperature and v_x, while v_y are within 12% of the exact solution.

Fig. 19 L^2 norm for Taylor-Green (*a*) temperature and (*b*) velocity

9 Conclusion

A total of six test cases were run, each one having an analytical solution, allowing for the determination of the SPH code's accuracy in simulating these different physics. Each test case was run multiple times with increasing resolution to determine the code's convergence rate, with the exception of the radiation cooling model, for which the volumetric cooling model is independent of particle resolution.

Section 3 examined the simulations of optically thin radiation of plasma using fixed properties and an equation of state. The SPH results indicated that both the table lookup and the radiation model are implemented properly, with radiation cooling from the exact (numerical integration of ordinary differential equation) and SPH models being nearly identical.

Section 4 investigated heat transfer simulations for cylindrical and spherical argon plasma. An L^2 analysis was conducted at 10, 30, and 100 μs. The relative error decreased as time progressed and the Fourier number approaches 1. At the lowest resolution, relative errors of 37.38%, 33.07%, and 8.75% were observed at 10, 30, and 100 μs, respectively. At the highest resolution examined, the relative errors were found to be 22.53%, 14.54%, and 2.22% observed at 10, 30, and 100 μs, respectively. The error was most significant near the boundary of the cylinder. The convergence rates were found to be $N^{-0.17}$, $N^{-0.28}$, and $N^{-0.47}$ at the same respective times.

Results of Couette flow simulations were presented in Sec. 5. The simulation of this problem examined the SPH code's accuracy in simulating viscous drag forces acting on fluid flow. A difficulty associated with simulating Couette flow in SPH is that the analytical solution assumes infinitely long geometry. To address this, a periodic boundary condition was utilized in these simulations, allowing for finite geometries to be used while also preventing the gas particles from being disrupted by vacuum end effects, which in turn would have degraded the accuracy of the numerical solution. This same technique was utilized in the simulations of the Gresho and Taylor-Green vortex in Secs. 6 and 8, respectively. The error for the flow velocity dropped from 15% to 0.105 m/s as resolution was increased. The convergence rate for the Couette flow simulations was found to be on the order of $N^{-0.38}$.

Oblique shocks are known to form [41,42] as a result of plasma jet merging in PLX. This makes oblique shock capturing another physics regime that the SPH code must accurately simulate. Simulation results of oblique shocks were examined in Sec. 7. An L^2 norm analysis was done for the postshock shock conditions. The error in temperature and density varied from 0.75% to 0.04% and 0.4% to 0.075%, respectively. The shock angle converged to within 0.39 deg of the correct answer. The convergence rates for the postshock density, temperature, and shock angle were found to be $N^{-0.46}$, $N^{-0.9}$, and $N^{-0.98}$, respectively.

Simulating the Gresho vortex in Sec. 6 demonstrated the code's accuracy in preserving angular momentum in fluid flow. This problem is known to be particularly difficult for SPH codes. The azimuthal velocity had an error ranging from 0.42 m/s to 0.36 m/s, and the pressure had an error ranging from 0.71 Pa to 0.63 Pa. The convergence rate of the Gresho vortex pressure was found on the order of $N^{-0.13}$, while the convergence rate for the azimuthal velocity is on the order of $N^{-0.1}$. These convergence rates are on the order of what has been reported in other SPH studies for this problem [37].

Finally, Sec. 8 examined the results of Taylor-Green vortex simulations. The Taylor-Green vortex offers a time-dependent solution of a decaying vortex, allowing for further assessment of the SPH code's accuracy in capturing the effects of viscous fluid flow. The error in the fluid velocity in the *x* and *y* directions both varied from 0.016 m/s to 0.01 m/s, while the pressure error varied from 3.89 Pa to 3.06 Pa. The convergence rates for the Taylor-Green pressure, and fluid velocity vectors in the *x* and *y* dimensions were found to be $N^{-0.1}$, $N^{-0.15}$, and $N^{-0.11}$, respectively.

The convergence rates for each of the test cases examined in this study were found to be on the order of convergence rates

reported in other SPH studies with an accuracy close to 10% of the exact solution. The implementation of SPFMax has enabled the researchers to conduct a large number of simulations pertinent to the ongoing PLX-α project, and the demonstrated 10% accuracy is crucial for simulating plasma liner formation and implosions in PLX studies. This in turn will aid in the design of future plasma-liner experiments.

Acknowledgment

Nomenclature

A = particle property
ARPA-E = Advanced Research Projects Agency-Energy
AW = atomic weight
C = convergence constant
C_v = heat capacity at constant volume, J/kg K
DOE = department of Energy
dr' = differential volume element
e = specific internal energy, J/kg
F_0 = Fourier modulus
h = radius of influence
k = thermal conductivity, W/m K
L = vector norm
M = Mach number
m_p = particle mass
MIF = magneto-inertial fusion
n = number of grid points
N = convergence rate
NASA = National Aeronautics and Space Administration
p = pressure, Pa
PJMIF = plasma jet magneto-inertial fusion
PLX = plasma liner experiment
r = particle position
$\bar{R}$ = universal gas constant
SPH = smoothed particle hydrodynamic
t = time
T = temperature
u = velocity, m/s
V = particle volume, m^3
Vx = Taylor-Green velocity in x direction, m/s
Vy = Taylor-Green velocity in y direction, m/s
W = smoothing kernel function
x_s = x-axis position in which 50% of peak pressure is located in postshock region
z_s = z-axis position in which 50% of peak pressure is located in postshock region
Z = plasma charge state

Greek Symbols

α = diffusivity
γ = specific heat ratio
δ = delta function
κ = smoothing function constant at a given location
λ = bulk viscosity coefficient
μ = viscosity coefficient
ξ = convergence value
Π = artificial viscosity
ρ = density, kg/m^3
σ = Stefan-Boltzmann constant
τ = deviatoric viscous stress tensor
χ = single group Planck emission opacity

Subscripts or Superscripts

e = electron
i = ion
r = ram
rad = radiation
s = shock

Units

eV = electron volt
K = kelvin
kJ = kilojoule
MA = mega amp
m/s = meters per second
ns = nanosecond
Pa = pascal
s = second
TW = terawatt
μs = microsecond

References

[1] Lindemuth, I., and Siemon, R., 2009, "The Fundamental Parameter Space of Controlled Thermonuclear Fusion," Am. J. Phys., **77**(5), pp. 407–416.
[2] Cassibry, J., Cortez, R., Stanic, M., Watts, A., Seidler, W., Adams, R., Statham, G., and Fabisinski, L., 2015, "Case and Development Path for Fusion Propulsion," J. Spacecr. Rockets, **52**(2), pp. 595–611.
[3] Lindemuth, I. R., and Kirkpatrick, R. C., 1983, "Parameter Space for Magnetized Fuel Targets in Inertial Confinement Fusion," Nucl. Fusion, **23**(3), pp. 263–284.
[4] Kirkpatrick, R. C., Lindemuth, I. R., and Ward, M. S., 1995, "Magnetized Target Fusion: An Overview," Fusion Technol., **27**(3), pp. 201–214.
[5] Miernik, J., Statham, G., Fabisinski, L., Maples, C., Adams, R., Polsgrove, T., Fincher, S., Cassibry, J., Cortez, R., Turner, M., and Percy, T., 2013, "Z-Pinch Fusion-Based Nuclear Propulsion," Acta Astronaut., **82**(2), pp. 173–182.
[6] Adams, R., Alexander, R., Chapman, J., Fincher, J., Philips, S., Polsgrove, A., Wayne, T., Patton, B., Statham, G., White, S., and Thio, Y., 2003, "Conceptual Design of In-Space Vehicles for Human Exploration of the Outer Planets," National Aeronautics and Space Administration, Washington, DC, Report No. 2003-212691.
[7] Slutz, S. A., Herrmann, M. C., Vesey, R. A., Sefkow, A. B., Sinars, D. B., Rovang, D. C., Peterson, K. J., and Cuneo, M. E., 2010, "Pulsed-Power-Driven Cylindrical Liner Implosions of Laser Preheated Fuel Magnetized With an Axial Field," Phys. Plasmas, **17**(5), p. 056303.
[8] Slutz, S. A., and Vesey, R. A., 2012, "High-Gain Magnetized Inertial Fusion," Phys. Rev. Lett., **108**(2), p. 025003.
[9] Gomez, M. R., Slutz, S. A., Sinars, D., Hahn, K. D., Hansen, S. B., Harding, E. C., Knapp, P. F., Schmit, P. F., Jennings, C. A., Awe, T. J., Geissel, M., Rovang, D., Chandler, G. A., Cooper, G. W., Cuneo, M. E., Harvey-Thompson, A. J., Herrmann, M. C., Hess, M. H., Johns, O., Lamppa, D. C., Marin, M. R., McBride, R. D., Peterson, K. J., Porter, J. L., Robertson, G. K., Rochau, G. A., Ruiz, C. L., Savage, M. E., Smith, I. C., Stygar, W. A., and Vesey, R. A., 2014, "Experimental Demonstration of Fusion-Relevant Conditions in Magnetized Liner Inertial Fusion," Phys. Rev. Lett., **113**(15), p. 155003.
[10] Thio, Y., Kirkpatrick, R., Knapp, C. E., Wysocki, F., Parks, P., and Schmidt, G., 1999, "Magnetized Target Fusion in a Spheroidal Geometry With Standoff Drivers," Current Trends in International Fusion Research—Second Symposium, Ottawa, ON, Canada, pp. 113–132.
[11] Hsu, S. C., Awe, T. J., Brockington, S., Case, A., Cassibry, J. T., Kagan, G., Messer, S. J., Stanic, M., Tang, X., Welch, D. R., and Witherspoon, F. D., 2012, "Spherically Imploding Plasma Liners as a Standoff Driver for Magnetoinertial Fusion," IEEE Trans. Plasma Sci., **40**(5), pp. 1287–1298.
[12] Samulyak, R., Parks, P., and Wu, L., 2010, "Spherically Symmetric Simulation of Plasma Liner Driven Magnetoinertial Fusion," Phys. Plasmas, **17**(9), p. 092702.
[13] Kim, H., Samulyak, R., Zhang, L., and Parks, P., 2012, "Influence of Atomic Processes on the Implosion of Plasma Liners," Phys. Plasmas, **19**(8), p. 082711.
[14] Hopkins, P. F., 2015, "A New Class of Accurate, Mesh-Free Hydrodynamic Simulation Methods," Mon. Not. R. Astron. Soc., **450**(1), pp. 53–110.
[15] Cassibry, J., Cortez, R., Hsu, S., and Witherspoon, F., 2009, "Estimates of Confinement Time and Energy Gain for Plasma Liner Driven Magnetoinertial Fusion Using an Analytic Self-Similar Converging Shock Model," J. Plasma Phys., **16**(11), p. 112707.
[16] Cassibry, J. T., 2004, "Numerical Modeling Studies of a Coaxial Plasma Accelerator as a Standoff Driver for Magnetized Target Fusion," Doctoral dissertation, University of Alabama in Huntsville, Huntsville, AL.
[17] Knapp, C. E., and Kirkpatrick, R. C., 2014, "Possible Energy Gain for a Plasma-Liner-Driven Magneto-Inertial Fusion Concept," Phys. Plasmas, **21**(7), p. 070701.
[18] Cassibry, J., Stanic, M., and Hsu, S., 2013, "Ideal Hydrodynamic Scaling Relations for a Stagnated Imploding Spherical Plasma Liner Formed by an Array of Merging Plasma Jets," Phys. Plasmas, **20**(3), p. 032706.

[19] Santarius, J. F., 2012, "Compression of a Spherically Symmetric Deuterium-Tritium Plasma Liner Onto a Magnetized Deuterium-Tritium Target," Phys. Plasmas, **19**(7), p. 072705.

[20] Awe, T., Adams, C. S., Davis, J. S., Hanna, D. S., Hsu, S. C., and Cassibry, J. T., 2011, "One-Dimensional Radiation-Hydrodynamic Scaling Studies of Imploding Spherical Plasma Liners," Phys. Plasmas, **18**(7), p. 072705.

[21] Davis, J. S., Hsu, S. C., Golovkin, I. E., MacFarlane, J. J., and Cassibry, J. T., 2012, "One-Dimensional Radiation-Hydrodynamic Simulations of Imploding Spherical Plasma Liners With Detailed Equation-of-State Modeling," Phys. Plasmas, **19**(10), p. 102701.

[22] Cassibry, J., Stanic, M., Hsu, S. C., Abarzhi, S. I., and Witherspoon, F. D., 2012, "Tendency of Spherically Imploding Plasma Liners Formed by Merging Plasma Jets to Evolve Toward Spherical Symmetry," Phys. Plasmas, **19**(5), p. 052702.

[23] Liu, G., and Liu, M., 2003, *Smoothed Particle Hydrodynamics: A Meshfree Particle Method*, World Scientific, Singapore.

[24] Monaghan, J., 2005, "Smoothed Particle Hydrodynamics," Rep. Prog. Phys., **68**(8), pp. 1703–1759.

[25] Hsu, S. C., Langendorf, S. J., Yates, K. C., Dunn, J. P., Brockington, S., Case, A., Cruz, E., Witherspoon, F. D., Gilmore, M. A., Cassibry, J. T., Samulyak, R., Stoltz, P., Schillo, K., Shih, W., Beckwith, K., and Thio, Y. C. F., 2017, "Experiment to Form and Characterize a Section of a Spherically Imploding Plasma Liner," IEEE Trans. Plasma Sci., **PP**(99), pp. 1–11.

[26] Rodriguez, M. A., and Cassibry, J. T., 2017, "A 3-D Smoothed-Particle Hydrodynamics Model of Electrode Erosion," IEEE Trans. Plasma Sci., **45**(11), pp. 3030–3037.

[27] Schillo, K. J., Cassibry, J. T., Rodriguez, M., and Thompson, S., 2016, "Test Suite for Hydrodynamic Modeling for Plasma Driven Magneto-Inertial Fusion," AIAA Paper No. 2016-4686.

[28] MacFarlane, J. J., Golovkin, I. E., and Woodruff, P. R., 2006, "HELIOS-CR—A 1-D Radiation-Magnetohydrodynamics Code With Inline Atomic Kinetics Modeling," J. Quant. Spectrosc. Radiat. Transfer, **99**(1–3), pp. 381–397.

[29] Fatehi, R., and Manzari, M. T., 2011, "Error Estimation in Smoothed Particle Hydrodynamics and a New Scheme for Second Derivatives," Comput. Math. Appl., **61**(2), pp. 482–498.

[30] Bonet, J., and Lok, T. S. L., 1996, "Variational and Momentum Preservation Aspects of Smooth Particle Hydrodynamic Formulation," Comput. Methods Appl. Mech. Eng., **180**(1–2), pp. 97–115.

[31] Watkins, S. J., Bhattal, A. S., Francis, N., Turner, J. A., and Whitworth, A. P., 1996, "A New Prescription for Viscosity in Smoothed Particle Hydrodynamics," Astron. Astrophys., **119**, pp. 177–187.

[32] Jeong, J. H., Jhon, M. S., Halow, J. S., and Osdol, J. V., 2003, "Smoothed Particle Hydrodynamics: Applications to Heat Conduction," Comput. Phys. Commun., **153**(1), pp. 71–84.

[33] Morris, J. P., Patrick, J. F., and Zhu, Y., 1997, "Modeling Low Reynolds Number Incompressible Flows Using SPH," J. Comput. Phys., **136**(1), pp. 214–226.

[34] Castor, J., 2004, *Radiation Hydrodynamics*, Cambridge University Press, Cambridge, UK, p. 368.

[35] Shampine, L. F., and Reichelt, M. W., 1997, "The MATLAB ODE Suite," SIAM J. Sci. Comput., **18**(1), pp. 1–22.

[36] VanSant, J. H., 1983, "Conduction Heat Transfer Solutions," Lawrence Livermore National Laboratory, CA, Report No. UCRL-52863-Rev.1.

[37] Zhu, Q., Hernquist, L., and Li, Y., 2015, "Numerical Convergence in Smoothed Particle Hydrodynamics," Astrophys. J., **800**(6), pp. 1–13.

[38] Anderson, J. D., 1991, *Fundamentals of Aerodynamics*, 2nd ed., McGraw-Hill, New York.

[39] Liska, R., and Wendroff, B., 2003, "Comparison of Several Different Schemes on 1D and 2D Test Problems for the Euler Equations," SIAM J. Sci. Comput., **25**(3), pp. 995–1017.

[40] Balsara, D., 2001, "Divergence-Free Adaptive Mesh Refinement for Magnetohydrodynamics," J. Comput. Phys., **174**(2), pp. 614–648.

[41] Merritt, E. C., Moser, A. L., Hsu, S. C., Loverich, J., and Gilmore, M., 2013, "Experimental Characterization of the Stagnation Layer Between Two Obliquely Merging Supersonic Plasma Jets," Phys. Rev. Lett., **111**(8), p. 085003.

[42] Merritt, E. C., Moser, A. L., Hsu, S. C., Adams, C. S., Dunn, J. P., Holgado, A. M., and Gilmore, M. A., 2014, "Experimental Evidence for Collisional Shock Formation Via Two Obliquely Merging Supersonic Plasma Jets," Phys. Plasmas, **21**(5), p. 055703.

[43] Anderson, J., 2003, *Modern Compressible Flow*, 3rd ed., McGraw-Hill, New York, Chap. 4.

[44] Hsu, S. C., Langendorf, S. J., Dunn, J. P., Yates, K. C., Gilmore, M. A., Witherspoon, F. D., Brockington, S., Case, A., Cruz, E., and Thio, Y. C. F., 2017, "Characterizing an Octant of a Spherically Imploding Plasma Liner as an MIF Driver," Bull. Am. Phys. Soc., **62**(12), p. BAPS.2017.DPP.T07.3

[45] Taylor, G. I., and Green, A. E., 1937, "Mechanism of the Production of Small Eddies From Larger Ones," Proc. R. Soc. London. Series A, **158**(895), pp. 499–521.

[46] DeBonis, J. R., 2013, "Solutions of the Taylor-Green Vortex Problem Using High-Resolution Explicit Finite Difference Methods," AIAA Paper No. 2013-0382.

[47] Kajzer, A., Pozorski, J., and Szwec, K., 2014, "Large-Eddy Simulations of 3D Taylor-Green Vortex: Comparison of Smoothed Particle Hydrodynamics, Lattice Boltzmann and Finite Volume Methods," J. Phys.: Conf. Ser., **530**(1), p. 012019.